Numerical Study of Transonic Flow Characteristics Around a Compound Delta Wing

Andrew T. Marion*◎ and Gaurav Sharma†◎

Kennesaw State University, Marietta, GA 30060, USA

This study numerically investigates the aerodynamic performance of a compound delta wing featuring multiple leading-edge sweep angles to optimize transonic flight characteristics. Inspired by the HAL Tejas wing design, the compound leading-edge configuration is designed to reduce wave drag while maintaining lift across a broad flight envelope. Computational fluid dynamics (CFD) simulations were performed at Mach numbers 0.75, 0.85, 0.95, 1.0, and 1.1, with angles of attack ranging from 0° to 55°. The unsteady Reynolds-averaged Navier–Stokes (URANS) approach, coupled with the Spalart–Allmaras turbulence model, was employed for its accuracy in resolving transonic aerodynamic flows at a reasonable computational cost. The numerical methodology was validated against experimental data through comparisons of surface pressure distributions and lift coefficients of delta wings. The aerodynamic performance of the compound delta wing was benchmarked against a baseline single-sweep delta wing to evaluate improvements in efficiency. Results reveal a notable reduction in drag, particularly at Mach 1, with decreases of 17.38%, 12.50%, and 13.25% at angles of attack of 5°, 30°, and 55°, respectively. While the maximum lift coefficient exhibited a slight reduction of 3.58%, the lift-to-drag ratio improved by 11.10%, 14.89%, and 7.24% at the same angles, demonstrating enhanced aerodynamic efficiency in the transonic regime. These findings highlight the potential of the compound delta wing configuration to improve transonic aircraft performance by mitigating drag penalties while preserving favorable lift characteristics.

Nomenclature

b	span
c	chord length
C_D	drag coefficient
C_L	lift coefficient
C_P	pressure coefficient
$\boldsymbol{g}$	gravity
M	mach number
p	static pressure
t	thickness of the wing
$\boldsymbol{u}$	velocity field
Greek	
α	angle of attack
μ	molecular dynamic viscosity
ν	molecular kinematic viscosity
ρ	density

I. Introduction

LOW-ASPECT-RATIO delta wings have been widely employed in supersonic aircraft, including civilian supersonic transports and fighter aircraft, due to their ability to minimize wave drag while maintaining sufficient low-speed maneuverability through vortex lift generation [1]. This lift mechanism is facilitated by the formation of two counter-rotating leading-edge vortices (LEVs) that develop as the wing operates at high angles of attack. These vortices induce a downward flow of air over the leading edge, accelerating the air and generating a low-pressure region on the upper surface of the wing, thereby enhancing lift [2]. However, as the angle of attack increases, vortex breakdown occurs, leading to unsteady aerodynamic loads and a significant loss of lift. This phenomenon is particularly pronounced in the transonic regime, where vortex breakdown occurs at lower angles of attack compared to subsonic

---

*Undergraduate Research Assistant, Department of Mechanical Engineering, Student Member AIAA.

†Assistant Professor, Department of Mechanical Engineering, Senior Member AIAA.

conditions [3]. Given that fighter aircraft primarily operate within the transonic regime, this limitation significantly restricts their flight envelope and maneuverability.

To mitigate these challenges, compound delta wings—characterized by multiple leading-edge sweep angles—have been proposed as a means to improve transonic aerodynamic performance. The variations in sweep angle along the leading edge modify vortex formation conditions, potentially delaying vortex breakdown and reducing the strength of shock waves forming over the wing. However, due to the intricate interplay of vortices and shock interactions at transonic speeds and high angles of attack, the flow behavior over compound delta wings remains highly complex and difficult to predict. Early aerodynamic models struggled to capture vortex formation at high angles of attack until advances in computational fluid dynamics (CFD) and numerical methodologies enabled more accurate simulations.

One of the earliest investigations into vortex flow in the transonic regime was conducted by Stanbrook and Squire [4], who examined flow separation over swept wings and determined that the angle of incidence at which flow separation occurred increased with Mach number in the transonic range. Later, Verhaagen et al. [5] performed experimental studies on vortex formation over a compound delta wing, revealing the presence of secondary vortices at high angles of attack. This phenomenon, attributed to the multi-sweep configuration, demonstrated the potential aerodynamic benefits of compound delta wings. At transonic speeds, shock formation and interactions play a critical role in vortex stability and breakdown.

Recent studies have employed computational approaches to examine vortex dynamics over compound delta wings. For instance, Ruetten and Zastrow [6] utilized unsteady Reynolds-averaged Navier–Stokes (URANS) simulations to investigate vortex interactions over a double-delta configuration, highlighting the unsteady nature of the flow at high angles of attack, where vortex evolution exhibits significant time-dependent behavior. Additionally, Werner et al. [7] analyzed a multi-swept delta wing in the transonic regime, observing cross-flow shock interactions with leading-edge vortices. The geometric definition of the sharp leading-edge compound delta wing investigated in the present study was established by Naimuddin et al. [8] and Sharma et al. [9], who applied steady-state RANS simulations to examine the aerodynamic characteristics across subsonic to supersonic flow regimes at angles of attack ranging from 0° to 15°.

The primary objective of this study is to characterize the flow behavior over a compound delta wing in the transonic regime, with a specific focus on leading-edge vortex formation, shock interactions, and vortex breakdown mechanisms. Key aspects under investigation include the location and intensity of leading-edge vortices, the influence of shock waves on vortex evolution, and the critical angle of attack at which vortex breakdown occurs. To achieve this, an unsteady compressible RANS numerical framework is employed to capture the time-dependent evolution of vortices at high angles of attack, providing insights into the complex aerodynamics of multi-swept delta wings.

By addressing these objectives, this study aims to advance the understanding of vortex dynamics and shock-vortex interactions in transonic flight, with direct implications for improving aerodynamic performance and expanding the operational flight envelope of future supersonic aircraft. The findings will contribute to the optimization of compound delta wing configurations, potentially reducing drag, mitigating vortex breakdown effects, and enhancing stability at transonic speeds—critical factors in the design of next-generation high-speed aircraft.

The article is structured as follows: Section II details the numerical setup and governing equations, beginning with a description of the geometry and computational domain, followed by an overview of the numerical methodology, including mesh structure, baseline parameters, fundamental conservation equations, and a mesh independence study. Section III presents a comprehensive analysis of the results, focusing on the aerodynamic performance and flow structures of the compound delta wing in comparison to the baseline delta wing, with particular emphasis on vortex dynamics, pressure distributions, and aerodynamic efficiency across transonic Mach numbers. Finally, Sec. IV summarizes the key research findings, discusses their implications, and provides recommendations for future studies on vortex control strategies and advanced aerodynamic optimizations for transonic flight applications.

II. Numerical Approach

A. Geometric Characterization and Computational Domain Specification

The geometric configuration utilized in this study is presented in Fig. 1. The wing features a flat plate configuration with an inboard sweep angle of 47° and an outboard sweep angle of 69°. A leading-edge kink is located at 39% of the chord, contributing to its aerodynamic characteristics. The model dimensions include a chord length (c) of 191 mm, a span of 206 mm, a thickness (t) of 10 mm, and a tip chord (c_t) of 30 mm. The wingtip is truncated at 161 mm along the chord, and the sharp leading edge is beveled at a 14° angle, while the trailing edge maintains a planar, blunt profile. The planform is inspired by the HAL Light Combat Aircraft (LCA) Tejas Mk 1 and was developed using

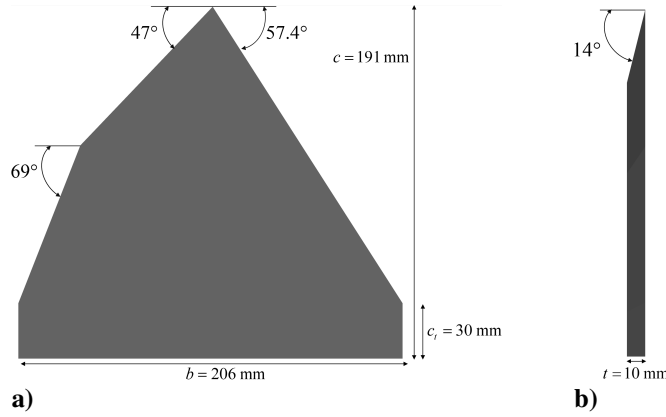American Institute of Aeronautics and Astronautics

Fig. 1. Schematic representation of a) the top-down view of the compound delta wing (left) and baseline delta wing (right) and b) the side view of both wing configurations.

Computer-Aided Design (CAD) software [10]. The baseline wing shares the same chord length, span, bevel angle, and thickness but features a different leading-edge sweep of 57.4%.

To ensure accurate aerodynamic predictions while minimizing computational overhead, an optimal computational fluid domain was established based on a domain independence study. The domain dimensions were defined relative to the root chord length (c), with an upstream boundary distance (L_U) of $7c$, a downstream boundary distance (L_D) of $15c$, and a lateral boundary distance of $5c$, as illustrated in Fig. 2. These dimensions ensure the simulation domain sufficiently encompasses the flow field while preventing artificial boundary interactions that could compromise the accuracy of the results. Additionally, the domain configuration was designed to maintain uniform flow conditions under varying angles of attack, thereby ensuring consistency across simulations. A watertight computational domain was employed to eliminate external interference, thereby enhancing the reliability of numerical predictions. The established domain was subsequently meshed to facilitate computational simulations, as discussed in the following section.

B. Mesh Configuration and Implementation

Following the geometric model and fluid domain construction, an unstructured meshing approach was adopted due to its adaptability to complex geometries, particularly in regions exhibiting sharp gradients and vortex interactions. Several mesh refinement techniques were employed, including edge and face sizing, to enhance resolution in critical regions such as the leading and trailing edges. To accurately resolve the boundary layer, an inflation layer was introduced along the wing surface. A systematic methodology was used to determine the first-layer height, total number of layers,
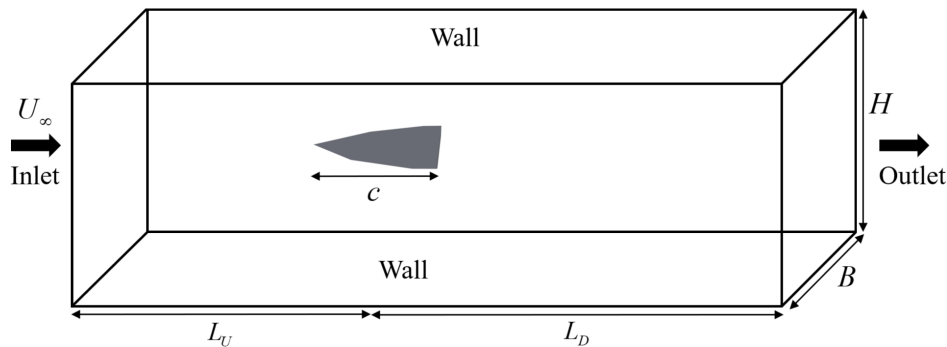

Fig. 2. An outline of the computational fluid domain used for the numerical investigations. In this context, *B* indicates the width, while *H* specifies the height of the domain.

and geometric growth rate, ensuring adequate boundary layer resolution. The total layer height was computed using:

$$Y_T = \sum_{K=0}^{N=1} Y_H G^K. \tag{1}$$

Ensuring proper boundary layer resolution is critical in aerodynamic studies. The boundary layer thickness (δ_{99}) near the freestream can be estimated as [11]:

$$\delta_{99} = Y_H \frac{(1 - G^N)}{(1 - G)}, \tag{2}$$

where Y_H is the first-layer thickness, G is the geometric growth ratio, and N is the total number of inflation layers. Recommended values for y^+ were maintained at 1 or 30, necessitating $N > 10$ and $N > 20$, respectively. A geometric growth ratio of 1.2 was employed, adhering to best practices to avoid excessive element expansion.

To ensure mesh quality and numerical accuracy, a mesh independence study was conducted. Five mesh resolutions were tested, with element counts ranging from 300,000 to 13.2 million cells, as shown in Table 1. The selected configuration, containing 3 million cells, exhibited an optimal balance between computational efficiency and accuracy, with a C_L error of 3.36%. The slight increase in error as mesh size is increased past 3 million can be attributed to round-off errors and rising skewness and aspect ratios at higher refinement levels. The final mesh ensured an average orthogonal quality near 1, with maximum skewness below 0.5, aligning with industry standards. The results of the mesh independence study, illustrating convergence behavior and accuracy trends across different mesh resolutions, are presented in Fig. 3, while the final mesh configuration is shown in Fig. 4.

C. Solution Setup and Boundary Conditions

The computational domain was imported into a finite volume solver [12], where the governing equations were discretized and solved using a three-dimensional, density-based, compressible, unsteady Reynolds-averaged Navier–Stokes (RANS) approach. The Spalart–Allmaras (SA) turbulence model [13] was selected due to its robustness and computational efficiency for high-angle-of-attack aerodynamic simulations. Its relatively simple one-equation formulation reduces computational cost compared to multi-equation turbulence models such as k-ω SST or Reynolds Stress Models (RSM), making it particularly well-suited for large-scale simulations where efficiency is critical. The SA model, a one-equation turbulence formulation, solves the transport equation for kinematic eddy viscosity ($\tilde{v}$):

$$\frac{\partial}{\partial t}(\rho \tilde{v}) + \frac{\partial}{\partial x_i}(\rho \tilde{v} u_i) = G_v + \frac{1}{\sigma_{\tilde{v}}} \left[\frac{\partial}{\partial x_j} \left\{ (\mu + \rho \tilde{v}) \frac{\partial \tilde{v}}{\partial x_j} \right\} + C_{b2\rho} \left(\frac{\partial \tilde{v}}{\partial x_j} \right)^2 \right] - Y_v + S_{\tilde{v}}, \tag{3}$$

where G_v is the production term, and $\sigma_{\tilde{v}}$, $C_{b2\rho}$, and $S_{\tilde{v}}$ are model constants and source terms, and Y_v represents the destruction of turbulent viscosity due to wall blocking and viscous damping, with v being the molecular kinematic viscosity.

The governing equations for the flow, encompassing continuity and momentum conservation, are expressed as follows:

$$\frac{\partial \rho}{\partial t} + \nabla \cdot (\rho \boldsymbol{u}) = 0, \tag{4}$$
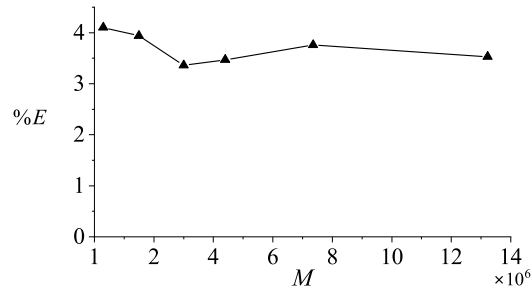

Fig. 3. Mesh sensitivity analysis for the base wing at $\alpha = 6.3°$.

Table 1. Mesh independence test

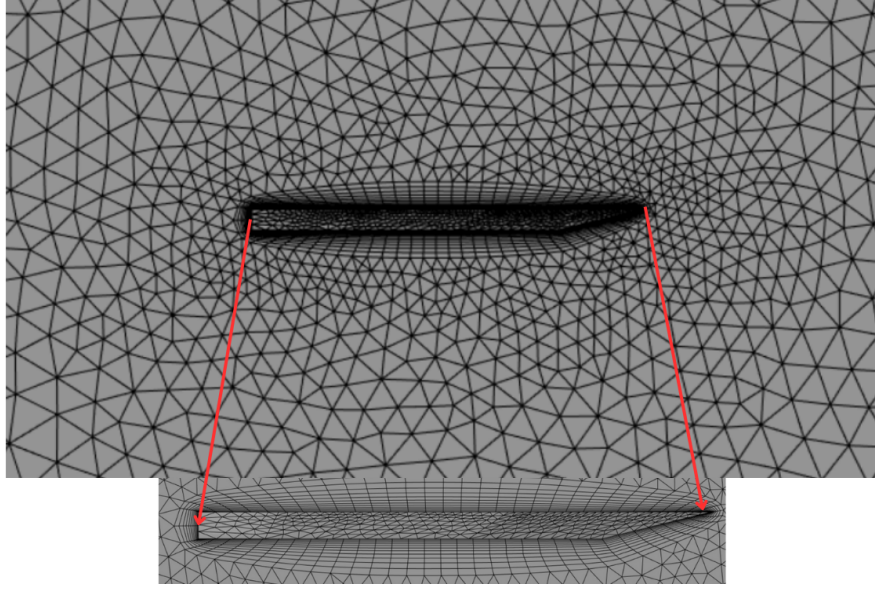| No of Elements (M)	C_L	C_L error
300,000	0.03435	4.10%
1,500,000	0.03430	3.94%
3,000,000	0.03411	3.36%
4,400,000	0.03414	3.47%
7,400,000	0.03424	3.76%
13,200,000	0.03416	3.53%

Fig. 4. Computational mesh surrounding the wing, accompanied by a detailed view of the inflation layers adjacent to the wing surface.

$$\frac{\partial \rho \boldsymbol{u}}{\partial t} + \nabla \cdot (\rho \boldsymbol{u}\boldsymbol{u}) = -\nabla p + \nabla \cdot (\overline{\overline{\tau}}) + \rho \boldsymbol{g} + \boldsymbol{F}, \tag{5}$$

where $\boldsymbol{u}$ represents the velocity field, p is the static pressure, $\rho \boldsymbol{g}$ and $\boldsymbol{F}$ correspond to the gravitational body force and external body forces, respectively. The stress tensor $\overline{\overline{\tau}}$ can be represented as:

$$\overline{\overline{\tau}} = \mu \left[(\nabla \boldsymbol{u} + \nabla \boldsymbol{u}^T) - \frac{2}{3} \nabla \cdot \boldsymbol{u} I \right], \tag{6}$$

where μ represents the molecular viscosity, I is the unit tensor, and the second term on the right-hand side accounts for volume dilation effects.

For the numerical solution, The flow was modeled as transient and compressible for Mach numbers of 0.75, 0.85, 0.95, 1.0, and 1.1. A pressure far-field boundary condition was prescribed at the inlet, while an atmospheric pressure outlet was imposed to facilitate natural flow development. The no-slip condition was enforced on the wing surface. An implicit solver was employed for numerical stability, and second-order upwind schemes were used for momentum, turbulence, and energy discretization. Gradient computations utilized a least-squares cell-based scheme to accurately capture secondary diffusion effects, while Roe-FDS (Flux Difference Splitting) method [14] was adopted for flux evaluation [11].

To ensure numerical accuracy, a convergence criterion of 10^{-6} was imposed on continuity, velocity components, and turbulence variables. Given the compressible nature of the transonic flow, the fluid density was computed using the ideal gas law, while viscosity was determined using Sutherland's law [15]. Due to the unsteady nature of vortex breakdown and shock interactions, a transient solver was employed with a time step of 10^{-4}, adhering to the Courant–Friedrichs–Lewy (CFL) criterion for stability.

This validated computational framework provides a robust and accurate representation of transonic flow over the compound delta wing, enabling a comprehensive analysis of leading-edge vortex formation, shock interactions, and vortex breakdown mechanisms.

III. Results and Discussion

A. Validation Study

To validate the numerical framework utilized in this study, a delta wing configuration was simulated and compared against experimental data obtained by Stallings Jr. and Lamb [16]. The validation was conducted using the geometric
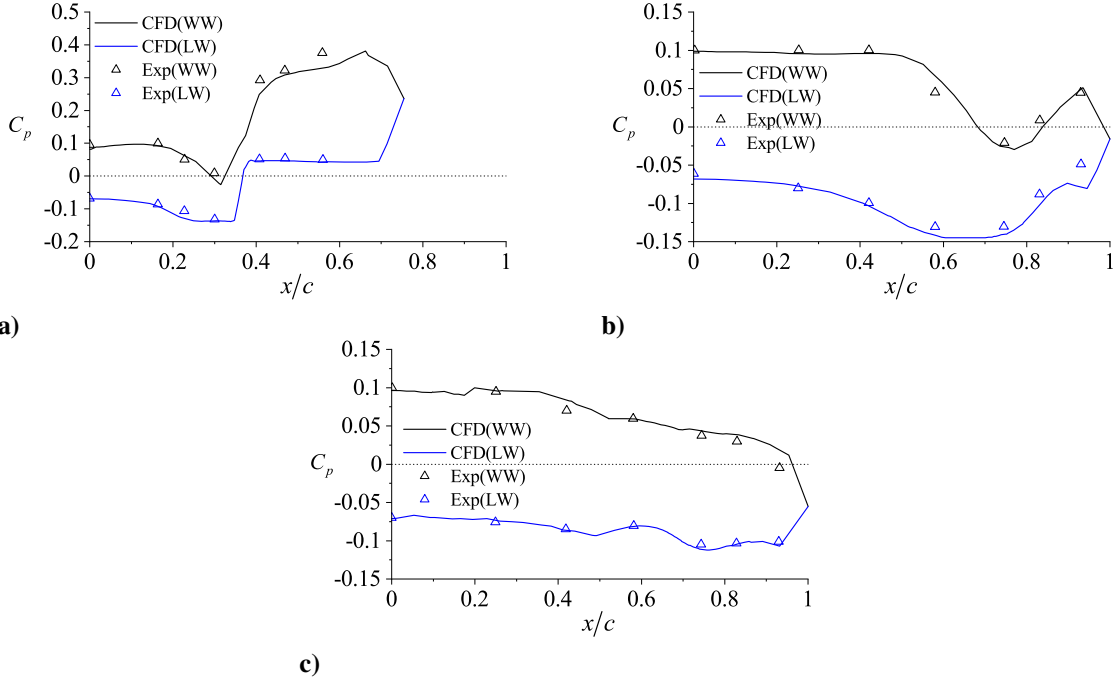
Fig. 5. Comparison of the computed pressure coefficient (C_p) with experimental data from Stallings Jr. and Lamb [16] for a standard delta wing at Mach 2.16 and an angle of attack of 6.3°. The validation is performed at three chordwise locations: a) $0.375c$, b) $0.625c$, and c) $0.844c$. In the legend, WW denotes the windward side, while LW represents the leeward side.

Table 2. Validation of computed lift coefficient with experimental data from Stallings Jr. and Lamb [16] across various angles of attack

Angle of Attack	C_L CFD	C_L Experimental	C_L error
1.3°	0.03411	0.033	3.36%
6.3°	0.16462	0.164	0.38%

parameters defined by Model Five in their study at a freestream Mach number of 2.16. The computed coefficient of pressure (C_p) values were compared at three locations along the chord at an angle of attack of 6.3°. As depicted in Fig. 5, the numerical results exhibit strong agreement with the experimental measurements, confirming the accuracy of the computational model in predicting surface pressure distributions.

Additionally, the lift coefficient (C_L) was evaluated at angles of attack of 1.3° and 6.3° and compared to the experimental data, as summarized in Table 2. The computed values demonstrate an average deviation of 1.87%, indicating that the numerical model effectively captures the aerodynamic performance of the delta wing. Based on this validation, the numerical approach was deemed reliable for further analysis.

B. Lift and Drag Coefficient Analysis

To investigate the aerodynamic performance of the base and compound delta wing configurations, lift and drag characteristics were analyzed across a range of angles of attack ($0° \leq \alpha \leq 55°$) at Mach numbers of 0.75, 0.85, 0.95, 1.0, and 1.1, as illustrated in Fig. 6. The upper limit of 55° was selected because the flow enters the post-stall regime beyond this point, where the accuracy of Reynolds-averaged Navier–Stokes (RANS) models deteriorates due to excessive turbulence-induced separation. At lower angles of attack ($\alpha \leq 10°$), C_L remains nearly identical for both wings across all Mach numbers, indicating minimal influence of the leading-edge modification in the attached flow regime. However, deviations emerge beyond $\alpha = 15°$, where the compound wing consistently generates lower lift than
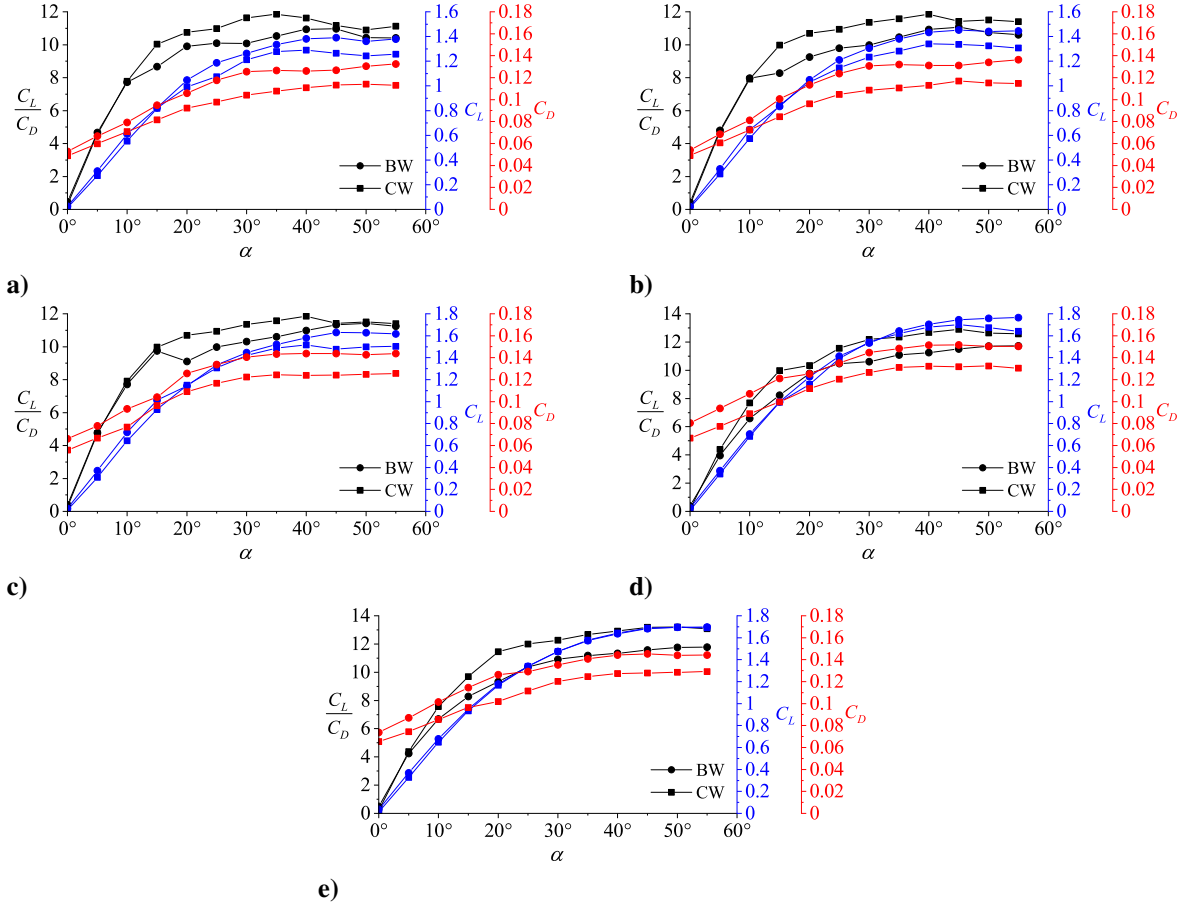
Fig. 6. Comparison of lift coefficient (C_L), drag coefficient (C_D), and the overall aerodynamic performance (C_L/C_D) between the compound delta wing and the baseline wing across five Mach numbers: a) 0.75, b) 0.85, c) 0.95, d) 1.0, and e) 1.1. The legend denotes BW as the baseline wing and CW as the compound delta wing.

the base wing due to differences in vortex strength and stability.

At $M = 0.75$ (Fig. 6a), the compound wing begins to diverge at $\alpha = 20°$, with a 5.3% reduction in C_L relative to the base wing. This difference increases at higher angles, with the compound wing reaching a peak C_L of 1.2887 at $\alpha = 40°$, compared to 1.3899 for the base wing at $\alpha = 45°$, representing a 7.3% decrease in peak lift. A similar trend is observed at $M = 0.85$ (Fig. 6b), where the compound wing exhibits a 7.8% lower maximum C_L and a 9.5% reduction at $\alpha = 55°$, suggesting earlier vortex breakdown and weaker vortex-induced suction due to the leading-edge modification. At $M = 0.95$ (Fig. 6c), the compound wing momentarily achieves comparable lift at $\alpha = 20°$ but falls behind at higher angles, with a 6.9% lower peak C_L and a 7.1% reduction at $\alpha = 55°$. At $M = 1.0$ (Fig. 6d), the compound wing reaches its peak lift at $\alpha = 45°$, while the base wing peaks later at $\alpha = 55°$), resulting in an overall 4.79% reduction in lift at high angles. At $M = 1.1$ (Fig. 6e), the impact of the leading-edge modification diminishes, with the compound wing closely follows the base wing's lift curve, and their peak C_L values differing by only 0.4%, indicating that compressibility effects dominate over vortex-induced lift mechanisms at higher transonic speeds. The observed reduction in C_L across most cases is attributed to premature vortex breakdown, as the leading-edge kink modifies the pressure distribution along the surface, destabilizing the primary vortex and inducing earlier flow separation. This effect is most pronounced at lower Mach numbers but weakens as the flow becomes more compressibility-dominated.

The drag coefficient (C_D) variation for both configurations across Mach numbers is presented in Fig. 6, showing that the compound wing consistently experiences lower drag than the base wing, with reductions becoming more pronounced at higher angles of attack. At $M = 0.75$ (Fig. 6a), the compound wing achieves a 7.48% reduction in minimum C_D at $\alpha = 0°$ and maintains lower drag across the angle-of-attack range, with a 14.7% decrease at $\alpha = 55°$, indicating delayed flow separation and improved vortex management. A similar trend is observed at $M = 0.85$ (Fig. 6b),

where the compound wing achieves up to a 16.0% reduction in drag at $\alpha = 25°$ and a maximum 10.8% decrease at $\alpha = 45°$, primarily due to reduced vortex-induced suction. At $M = 0.95$ (Fig. 6c), drag reductions remain consistent, reaching 18.0% at $\alpha = 10°$ and averaging 13.1% lower drag across all angles, suggesting better flow attachment and reduced separation effects. At $M = 1.0$ (Fig. 6d), the compound wing exhibits a 16.9% and 10.7% drag reduction at $\alpha = 10°$ and $\alpha = 20°$, respectively, while also mitigating shock-induced wave drag at transonic speeds. At $M = 1.1$ (Fig. 6e), drag reductions stable, with 15.7% lower C_D at $\alpha = 15°$ and 13.8% at $\alpha = 40°$, reinforcing the compound delta wing's ability to reduce both vortex-induced and wave drag. These findings confirm that the compound delta wing provides an aerodynamic advantage in transonic applications, where minimizing drag is a key design objective.

The aerodynamic efficiency, represented by the lift-to-drag ratio (C_L/C_D), is shown in Fig. 6 for both wing configurations across Mach numbers. In general, the compound wing demonstrates superior efficiency at moderate to high angles of attack due to its reduced drag, despite generating slightly lower lift in most cases. At $M = 0.75$ (Fig. 6a), the compound wing achieves up to 12.6% higher efficiency than the base wing, with a peak C_L/C_D of 11.8506 at $\alpha = 35°$. At $M = 0.85$ (Fig. 6b), its efficiency advantage persists, with a maximum improvement of 20.5% at $\alpha = 15°$. At $M = 0.95$ (Fig. 6c), the compound wing maintains a 11.4% higher peak efficiency, reaching 12.2429 at $\alpha = 40°$. The trend continues at $M = 1.0$ (Fig. 6d), where the compound wing achieves 12.6377 at $\alpha = 50°$, outperforming the base wing by 12.1%. The most pronounced gains occur at $M = 1.1$ (Fig. 6e), where the compound wing reaches a maximum C_L/C_D of 13.20 at $\alpha = 50°$, a 12.0% improvement over the base wing. Across all cases, the compound wing consistently demonstrates higher aerodynamic efficiency, with gains ranging from 7.24% to 13.57%, highlighting its potential benefits in transonic applications where drag reduction is critical. This improvement is primarily attributed to significant drag reduction without a proportional loss in lift, making the compound wing a viable design for transonic flight where maintaining efficiency is crucial.
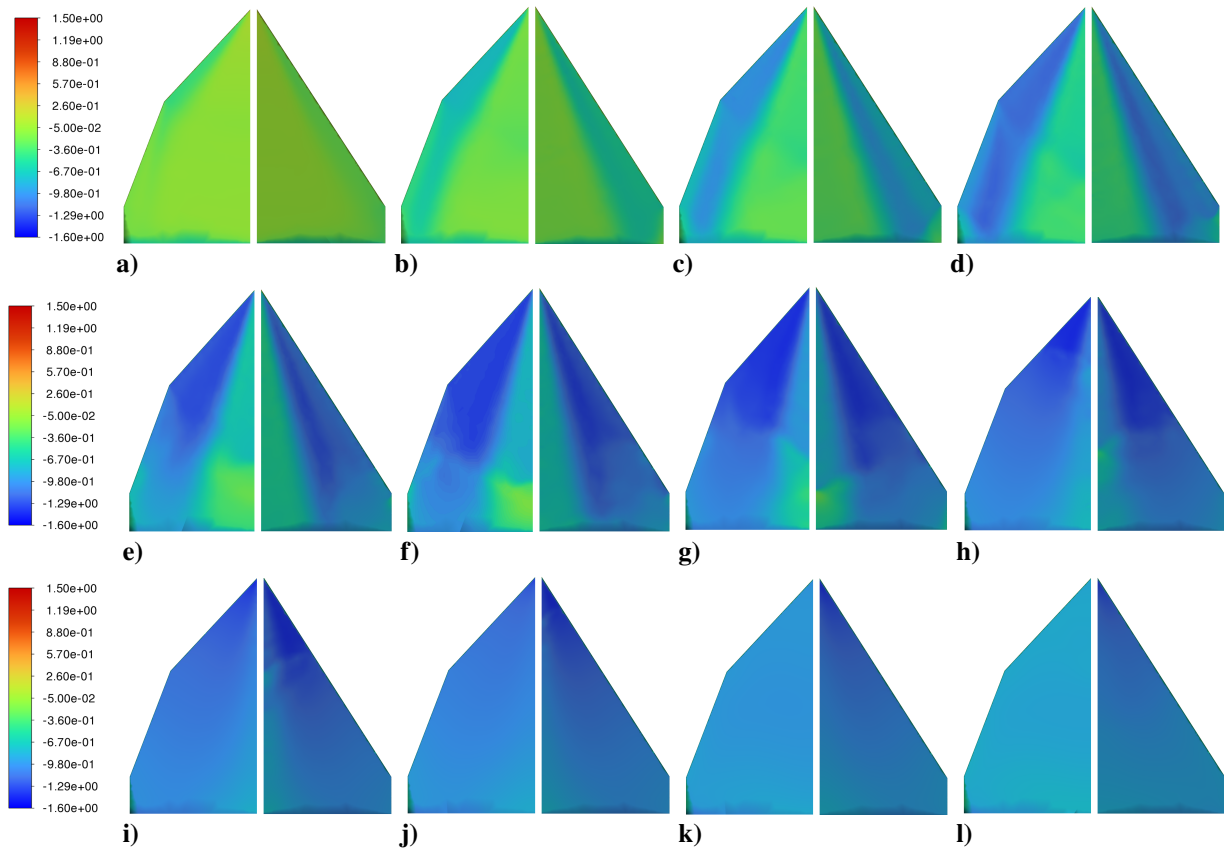

Fig. 7. Comparison of the pressure coefficient (C_p) distribution over the upper surface of the compound wing (left) and the base wing (right) at $M = 1.0$ across twelve angles of attack: a) $\alpha = 0°$, b) 5°, c) 10°, d) 15°, e) 20°, f) 25°, g) 30°, h) 35°, i) 40°, j) 45°, k) 50°, and l) 55°.

C. Evaluation of Pressure Contours and Flow Distribution

To further analyze the aerodynamic behavior of the base and compound wings, pressure contours were examined for angles of attack ranging from 0° to 25° at $M = 1.0$, providing insights into the influence of the compound wing geometry on vortex formation and flow characteristics. As shown in Fig. 7, at $\alpha = 0°$ (Fig. 7a), both wings exhibit minimal vortex formation, with largely uniform pressure distribution. However, the compound wing produces a smaller low-pressure region near the leading edge, whereas the base wing generates a larger, more intense low-pressure region, indicating its stronger dependence on angle of attack for lift generation. At $\alpha = 5°$ (Fig. 7b), the primary vortex initiates at the apex of the leading edge. On the compound wing, this vortex is strongest near the front and weakens downstream, whereas on the base wing, the vortex grows in strength along the chord, leading to a more pronounced pressure drop. This behavior is likely due to the compound wing's initial lower sweep angle, which promotes earlier vortex formation but results in subsequent decay due to the increased sweep angle at the kink.

At higher angles of attack ($\alpha = 10°$ and $15°$), vortex intensity increases, as evident from the decreasing C_P and expansion of the vortex region. At 10° (Fig. 7c), crossflow shock waves begin to emerge over the compound wing at the leading-edge kink, propagating downstream. By 15° (Fig. 7d), these shocks intensify, causing a localized pressure rise near 70% chord, further influencing vortex evolution. At $\alpha = 20°$ (Fig. 7e) and 25° (Fig. 7f), the vortex structure continues to grow, but incipient flow separation is observed on the compound wing at approximately 50%–70% chord, whereas the base wing maintains attached flow. This premature separation is likely responsible for the compound wing's lower $C_{L_{max}}$. Beyond 30°, vortex breakdown occurs over both wings (Figs. 7g and 7h), followed by complete flow separation at $\alpha \geq 40°$ (see Figs. 7i–7l). These findings reinforce that while the compound wing modifies vortex formation dynamics, it also induces earlier vortex breakdown, reducing its lift potential at higher angles of attack.

D. Isosurface and Velocity Distribution Analysis

To further examine the vortex structures and their development over the base and compound delta wings, the swirling strength isosurface and velocity contours along vertical planes were analyzed. These visualizations provide crucial insights into vortex formation, stability, and breakdown mechanisms. The swirling strength isosurface was evaluated at $M = 1.0$ and $\alpha = 15°$ to assess vortex coherence, while velocity contours were examined at the same flow conditions to study crossflow characteristics and vortex evolution. Figure 8 presents the swirling strength isosurface over the two wings. Both the compound wing (Fig. 8a) and base wing (Fig. 8b) exhibit leading-edge vortex formation, a well-known characteristic of highly swept delta wings. However, key differences emerge in vortex evolution. The compound wing shows regions of higher swirling strength concentrated toward the aft section, indicating increased vortex decay as the flow progresses downstream. This accelerated decay is associated with the gradual weakening of the primary vortex, leading to earlier onset of vortex breakdown. Additionally, as the flow detaches from the wing surface, the vortex structures dissipate into the freestream, which correlates with the observed reduction in $C_{L_{max}}$ for the compound wing. For highly swept delta wings, the separation at the leading edge induces the formation of counter-rotating vortices, which appear as circular structures when analyzed along crossflow planes perpendicular to the span. The interaction of the primary vortex with the upper surface boundary layer influences secondary vortex formation, which plays a crucial role in flow stability and lift enhancement.

Figure 9 illustrates velocity contours at three distinct chordwise locations. At 25% of the chord (Fig. 9a), the
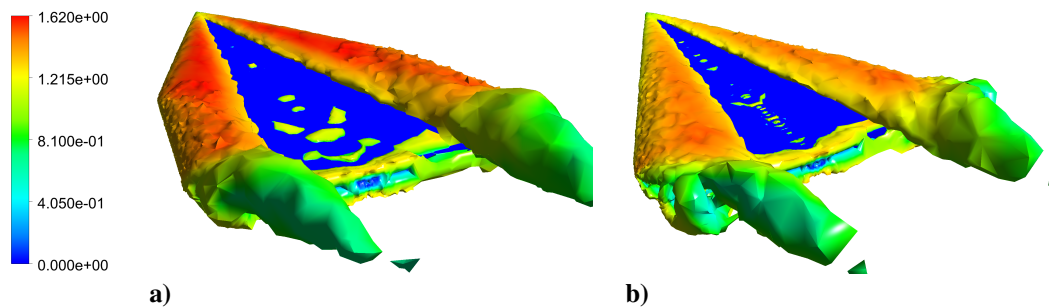

Fig. 8. Isosurface representation of swirling strength, colored by Mach number, for a) the compound delta wing and b) the baseline delta wing at $M = 1.0$ and $\alpha = 15°$.
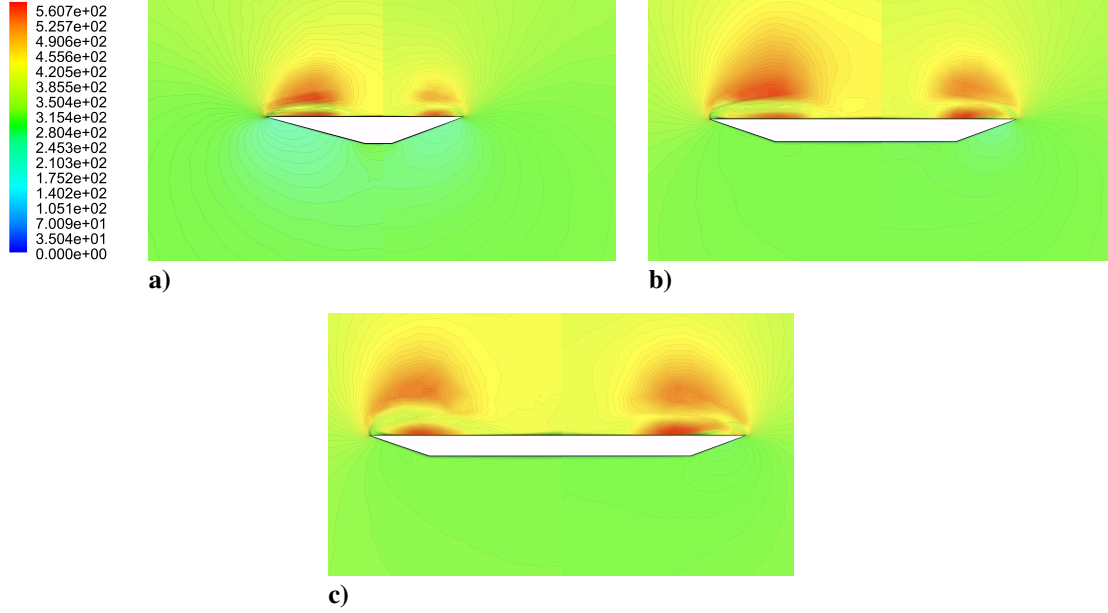
Fig. 9. Velocity contours [m/s] on perpendicular planes showing vortex formation over the compound wing (left) and base wing (right) at a) 25%, b) 50%, and c) 75% of the chord for $M = 1.0$ and $\alpha = 15°$.

initiation of the leading-edge vortex is evident. The compound wing exhibits a more intense vortex compared to the base wing, resulting in a more forward-shifted low-pressure region, as seen in the C_p distributions (Fig. 5). At 50% chord (Fig. 9b), the compound wing continues to exhibit a stronger primary vortex, while the base wing develops a more distinct secondary vortex beneath the primary vortex. This difference highlights a key deviation from conventional delta wing flow behavior, where the compound wing largely suppresses the secondary vortex formation.

At 75% chord (Fig. 9c), the vortex structure over the compound wing begins to disintegrate, indicating premature vortex breakdown. This breakdown is observed as a loss of vortex coherence and a reduction in velocity magnitude within the vortex core. In contrast, the base wing retains a well-defined vortex system, with both primary and secondary vortices strengthening downstream. The earlier onset of vortex breakdown in the compound wing aligns with its observed lower $C_{L_{max}}$ compared to the base wing, suggesting that while the compound wing reduces drag, it compromises vortex stability, resulting in reduced peak lift performance.

IV. Concluding Remarks

This study presents a comprehensive numerical investigation into the aerodynamic performance and flow structures of a compound delta wing featuring multiple leading-edge sweeps at transonic speeds. The results demonstrate a significant reduction in drag and an increase in aerodynamic efficiency, particularly at moderate to high angles of attack, confirming the benefits of the compound leading-edge design. Numerical simulations, conducted using unsteady Reynolds-averaged Navier–Stokes (URANS) equations with Spalart–Allmaras turbulence model, provided key insights into the effects of the compound wing geometry on vortex dynamics, pressure distributions, vortex breakdown, and overall aerodynamic performance.

The findings indicate that the compound wing produces a forward-shifted primary vortex with reduced secondary vortex formation, contributing to altered vortex evolution and earlier vortex breakdown. Additionally, shock interactions at the leading-edge kink play a crucial role in modifying vortex behavior, further influencing aerodynamic performance. While the compound wing enhances efficiency and reduces drag, its susceptibility to premature vortex breakdown affects its lift characteristics at high angles of attack.

Future research will expand this analysis to post-stall flow regimes using large eddy simulations (LES) to further investigate vortex instability and breakdown mechanisms. Additionally, active flow control strategies, such as suction and blowing jet nozzles and plasma-based flow control, will be explored to mitigate vortex breakdown and improve stall resistance. These advancements will contribute to a more complete understanding of multi-swept delta wing

aerodynamics and inform future aircraft design optimizations for transonic flight applications.

Acknowledgements

References

[1] Lee, S., "A Cross Flow Vortex Model of Delta Wings," *AIAA AVIATION 2023 Forum*, AIAA Paper 2023-3751, June 2023. doi:10.2514/6.2023-3751.

[2] Ericsson, L., "Delta Wing Vortex Breakdown Dynamics," *33rd Aerospace Sciences Meeting and Exhibit*, AIAA Paper 1995-367, January 1995. doi:10.2514/6.1995-367.

[3] Bannink, W., Houtman, E., and Ottochian, S., "Investigation of the Vortex Flowover a Sharp-edged Delta Wing in the Transonic Speed Regime," Technical Report, Delft University of Technology, 1989.

[4] Stanbrook, A. and Squire, L. C., "Possible Types of Flow at Swept Leading Edges," *Aeronautical Quarterly*, Vol. 15, No. 1, February 1964, pp. 72–82. doi:10.1017/s0001925900003024.

[5] Verhaagen, N., Jenkins, L., Kern, S., and Washburn, A., "A Study of the Vortex Flow Over a 76/40-deg Double-Delta Wing," *33rd Aerospace Sciences Meeting and Exhibit*, AIAA Paper 1995-650, January 1995. doi:10.2514/6.1995-650.

[6] Ruetten, M. and Zastrow, J., "Vortex Interaction, Vorticity Flux and Torsion Over a Generic Double-Delta Wing Configuration," *AIAA AVIATION 2022 Forum*, AIAA Paper 2022-3994, June 2022. doi:10.2514/6.2022-3994.

[7] Werner, M., Schütte, A., and Weiss, S., "Turbulence Model Effects on Vortex Interaction Prediction on a Multiswept Delta Wing," *Journal of Aircraft*, Vol. 61, No. 1, January 2024, pp. 211–221. doi:10.2514/1.c037421.

[8] Naimuddin, M., Chopra, G., and Sharma, G., "Experimental & Computational Study on Compound Delta Wing," *Journal of Basic and Applied Engineering Research*, Vol. 1, No. 3, October 2014, pp. 47–52.

[9] Sharma, G., Naimuddin, M., Chopra, G., Sinha, J., and Sharma, G., "Numerical Analysis of Flow Field Over Compound Delta Wing at Subsonic and Supersonic Speeds," *2016 IEEE Aerospace Conference*, Vol. 1, Big Sky, Montana, March 2016, pp. 1–20. doi:10.1109/aero.2016.7500662.

[10] Dassault Systemes, "SolidWorks, Release 2024 SP5," 2024.

[11] ANSYS Inc., Southpointe, 275 Technology Drive, Canonsburg, PA, *ANSYS Fluent User's Guide*, 15th ed., November 2013.

[12] ANSYS, "Fluent, Release 2023 R2, Version 23.2," 2023.

[13] Spalart, P. and Allmaras, S., "A One-Equation Turbulence Model for Aerodynamic Flows," *30th Aerospace Sciences Meeting and Exhibit*, AIAA Paper 1992-439, January 1992. doi:10.2514/6.1992-439.

[14] Roe, P., "Approximate Riemann Solvers, Parameter Vectors, and Difference Schemes," *Journal of Computational Physics*, Vol. 43, No. 2, October 1981, pp. 357–372. doi:10.1016/0021-9991(81)90128-5.

[15] Sutherland, W., "LII. The Viscosity of Gases and Molecular Force," *The London, Edinburgh, and Dublin Philosophical Magazine and Journal of Science*, Vol. 36, No. 223, December 1893, pp. 507–531. doi:10.1080/14786449308620508.

[16] Stallings Jr., R. L. and Lamb, M., "Wing-Alone Aerodynamic Characteristics for High Angles of Attack at Supersonic Speeds," Technical Report NASA-TP-1889, NASA, 1981.